energies

MDPI

Article

Numerical Simulation and Structural Optimization of Flow and Heat Transfer of Flue Gas from Ascharite Ore Roasting in a CFB Desulfurization Reactor

Mingjie Feng [1,2,*], Dedong Li [1], Shiwei Yu [1] and Zhuo Wang [1]

[1] School of Metallurgy, Northeastern University, Shenyang 110819, China; ldd2001x@163.com (D.L.); ysw0901302@163.com (S.Y.); 15698842133@163.com (Z.W.)
[2] Liaoning Engineering Research Center of Process Industry Energy Saving and Low-Carbon Technologies, Shenyang 110819, China
* Correspondence: fengmj@epm.neu.edu.cn

Abstract

This study employs numerical simulation methods to systematically analyze the multiphase flow and heat transfer characteristics in a circulating fluidized bed flue gas desulfurization (CFB-FGD) reactor handling ascharite ore roasting flue gas. Based on the simulation results, key structural optimization strategies are proposed. A three-dimensional mathematical model was developed based on the Fluent 19.1 platform, and the multiphase flow process was simulated using the Eulerian-Lagrangian method. The study examined the effects of venturi tube structure, atomized water nozzle installation height, and gas injection disruptor configuration on reactor performance. Optimization strategies for key structural components were systematically evaluated. The results show that the conventional inlet structure leads to significant non-uniformity in the velocity field. Targeted adjustments to the dimensions of venturi tubes at different positions markedly improve the velocity distribution uniformity. Reducing the atomized water nozzle installation height from 1.50 m to 0.75 m increased the temperature distribution uniformity index in the middle part of the straight pipe section by 5.5%. Moreover, a gas injection disruptor was installed in the upper part of the straight pipe section of the CFB-FGD reactor. Increasing the gas injection velocity from 15 m/s to 30 m/s increased the average residence time of desulfurization sorbents by 17.0%. This increase effectively enhances gas–solid mixing within the CFB-FGD reactor. The optimization strategies described above significantly reduced the extent of flow dead zones and low-temperature regions in the CFB-FGD reactor and improved flow conditions. This study provides important theoretical and technical support for the optimization and industrial application of CFB-FGD technology for ascharite ore roasting flue gas.

Keywords: CFB-FGD reactor; ascharite ore; roasting; numerical simulation; structural optimization

Check for updates

Academic Editor: Artur Blaszczuk

Received: 3 November 2025
Revised: 20 December 2025
Accepted: 22 December 2025
Published: 19 January 2026

Copyright: © 2026 by the authors. Licensee MDPI, Basel, Switzerland. This article is an open access article distributed under the terms and conditions of the Creative Commons Attribution (CC BY) license.

1. Introduction

Ascharite ore is a critical raw material for the production of boric acid, borax, borate salts, boron oxide, and boron nitride. These products are widely used in the light industry, construction materials, metallurgy, and aerospace [1]. The eastern region of Liaoning Province is China's most significant area rich in ascharite ore and has long served as a

traditional mining hub. Notably, the Wengquangou deposit in Fengcheng hosts a world-class ascharite ore reserve, containing an estimated 21.85 million tonnes of B_2O_3 [2,3]. Over several decades, China's ascharite ore processing technologies have evolved from a singular acid-based approach to a diversified and advanced system. This evolution includes techniques such as pressure-alkali leaching, the carbon-alkali method, and combined alkali processes, marking technological maturity [4–7]. However, regardless of the chosen processing method, high-temperature roasting of the raw ore in air remains an essential preliminary step.

The roasting of ascharite ore aims to disrupt its crystal structure and eliminate crystalline water, thereby transforming the ore into a loose and porous state. This structural modification enhances the chemical reactivity of the ore and facilitates the subsequent leaching of B_2O_3 [8,9]. Common roasting equipment includes rotary kilns, vertical furnaces, fluidized beds, and bubbling beds [10]. The primary component of ascharite ore is fibrous ascharite, accompanied by appreciable amounts of serpentine and magnetite. Minor impurities include dolomite, chlorite, talc, mica, and pyrite. During the roasting process, the generated flue gas contains various components, including N_2, CO_2, H_2O, CO, O_2, particulate matter, and trace amounts of SO_2 and volatilized B_2O_3. The concentrations of these pollutants often significantly exceed national emission standards. Among these pollutants, SO_2 is of particular concern as a major contributor to acid rain and poses substantial risks to the ecological environment. Additionally, SO_2 exposure can cause adverse health effects, including respiratory disorders and hematological diseases [11,12]. Therefore, effective desulfurization technologies must be employed to ensure that emissions from the roasting of ascharite ore comply with environmental regulations.

The fundamental principle of flue gas desulfurization is based on the chemical reaction between sulfur dioxide (SO_2) and alkaline sorbents. Based on the presence of water during the process and the physical state of the desulfurization products, flue gas desulfurization technologies are typically classified into wet, semi-dry, and dry methods [13,14]. Wet FGD is a relatively traditional method with high desulfurization efficiency and mature technology. However, it has drawbacks such as severe equipment corrosion and difficult wastewater treatment. The main wet FGD processes include the limestone-gypsum process, ammonia-based process, sodium alkali process, seawater process, and double alkali process [15–17]. Dry desulfurization employs dry powdered sorbents to react with SO_2 under anhydrous conditions. Although this method typically results in lower sorbent utilization and desulfurization efficiency, it offers advantages such as more manageable byproducts and milder equipment corrosion. Common dry processes include activated carbon adsorption, electron beam irradiation, charged dry sorbent injection, and microwave-assisted methods [18–21]. Semi-dry desulfurization integrates the benefits of both wet and dry methods. The main reaction occurs in a moist environment, while the final products remain in a dry state. This approach enables fast reaction kinetics, high desulfurization efficiency, and easier handling of solid residues. Typical semi-dry processes include spray drying and circulating fluidized bed technologies [22–24]. Therefore, selecting an appropriate desulfurization technology requires balancing technical performance, environmental impact, economic viability, and operational conditions.

Currently, most of the flue gas generated from the roasting of ascharite ore in eastern Liaoning Province, China, is treated using wet desulfurization technology. However, with ongoing advancements in ascharite roasting processes and increasingly stringent environmental regulations, the limitations of wet desulfurization have become more pronounced [25,26]. These limitations include equipment corrosion and challenges in wastewater treatment. Consequently, semi-dry desulfurization technology has garnered growing

attention as a promising alternative. This technology offers high SO_2 removal efficiency and produces solid byproducts that are easier to manage.

CFB-FGD technology is a representative semi-dry desulfurization process, originally developed and commercialized by the German company Lurgi in the 1980s [27]. Over decades of refinement, this technology has undergone substantial improvements in desulfurization performance, process systems, and applicability, achieving ultra-low emission levels. However, despite its excellent performance in conventional coal-fired flue gas desulfurization, CFB-FGD is not directly suitable for treating flue gas generated from the roasting of ascharite ore. This is primarily because the composition of ascharite roasting flue gas is distinct from that of typical coal combustion flue gas. In particular, it contains significantly higher concentrations of particulate matter and B_2O_3 vapor [28,29]. In conventional desulfurization reactors, B_2O_3 vapor tends to condense and adhere to surfaces, where it reacts with $CaSO_3$ or CaO to form $Ca_3(BO_3)_2$ hard scale. This leads to wall fouling and disrupts sorbent fluidization. Additionally, other challenges can hinder gas–solid heat transfer. These include low turbulence intensity in the upper flue gas region and insufficient residence time of the desulfurization sorbents. These factors reduce desulfurization efficiency within the fluidized bed [30,31]. These issues highlight the necessity for structural optimization of conventional desulfurization reactors. Such optimization is essential for adapting the CFB-FGD reactor to ascharite ore flue gas treatment. Computational Fluid Dynamics (CFD), a powerful and widely validated numerical simulation tool, was employed to analyze this complex system [32,33].

This study aims to develop a coupled mathematical and physical model for multiphase flow and heat transfer within a CFB-FGD reactor. The model specifically addresses ascharite ore roasting flue gas, which contains roasting product particles and dust. This study was conducted using the Fluent 19.1 numerical simulation platform. The optimization strategies include three main approaches: modifying the venturi tube bundle structure, adjusting the atomized water nozzle installation height, and installing a gas injection disruptor in the upper part of the straight pipe section. These measures aim to improve the uniformity of flow and temperature fields within the reactor, enhance flue gas turbulent mixing, and increase the residence time of the desulfurization sorbents. The ultimate goals are to suppress borate deposition and improve the capability of CFB-FGD technology for treating complex flue gas. Due to limited understanding of the interaction mechanisms between flue gas components and desulfurization sorbents, this study does not incorporate detailed chemical reaction modeling.

2. Model Description

2.1. Physical Model

The ascharite ore used in this study was extracted from the Fengcheng Wengquangou deposit in Liaoning Province, China. Based on compositional analysis, the average contents of the main elements in the raw ore are listed in Table 1. The roasting process employs a rotary kiln equipped with a single KFS-type burner mounted on the discharge end. The fuel used is low-sulfur pulverized coal, and combustion air is supplied using ambient air. Before roasting, the ore is crushed and screened to a particle size range of 5–25 mm. The maximum roasting temperature reaches 1120 K, and the maximum flue gas flow rate is 21,000 m^3/h. The thermophysical properties of the roasting flue gas, measured under actual operating conditions, are summarized in Table 2.

Table 1. Average content of major elements in ascharite ore (mass %).

B_2O	CaO	MgO	Fe_2O_3	Al_2O_3	SiO_2	S	Loss in Ignition
9.73	6.79	32.61	2.23	1.08	20.28	0.15	27.13

Table 2. Properties of the roasting flue gas [1].

T, K	ρ_f, kg/m^3	$c_{p,f}$, kJ/(kg·K)	λ, W/(m·K)	α, m^2/s	μ, Pa·s	Pr
273.15	1.293	1.041	0.0228	16.9×10^{-6}	15.8×10^{-6}	0.72
373.15	0.951	1.065	0.0313	30.8×10^{-6}	20.4×10^{-6}	0.69
473.15	0.747	1.098	0.0401	48.9×10^{-6}	24.5×10^{-6}	0.67

[1] The parameters in the table were measured under atmospheric pressure. The mass fractions of the main components in the flue gas are: w_{CO_2} = 0.13, w_{H_2O} = 0.13, w_{N_2} = 0.74. Other components are converted to standard conditions. Under the condition of 6% oxygen content, the dry basis concentrations are as follows: SO_2: 15,700–18,000 mg/m^3, H_2S: 220–320 mg/m^3, B_2O_3: 1200–1500 mg/m^3, and dust (dry basis, particle diameter: 2.5–450 μm): 350–500 mg/m^3.

As shown in Table 2, the roasting flue gas emitted from the rotary kiln exceeds national emission standards and must be purified before discharge. To address this, a CFB-FGD system is installed downstream of the rotary kiln to treat the non-compliant emissions, as illustrated in Figure 1. The roasting flue gas first enters a venturi tube at the bottom of the CFB-FGD reactor, where it is straightened and accelerated before entering the conical diffuser section. The sorbents (lime, quicklime, or slaked lime slurry) and atomized water droplets are injected through the diffuser section. They mix with the flue gas and form a highly turbulent fluidized bed in the straight pipe section of the reactor. During the initial stage, atomized water creates a thin liquid film on the sorbent surface, into which SO_2 dissolves and reacts ionically with $Ca(OH)_2$. As the reaction proceeds, inert byproducts begin to accumulate on particle surfaces, impeding further reaction. However, the strong turbulence within the bed promotes frequent collisions among particles, which cause the reaction product layers to abrade and peel off, thereby exposing fresh reactive surfaces and sustaining a high desulfurization rate. As the liquid film evaporates, the temperature of the flue gas gradually decreases, and SO_2 continues to react directly with the exposed surfaces of the dry sorbents, although with lower reaction efficiency. Finally, the flue gas, along with reaction products and unreacted sorbent, exits the top of the reactor and enters a cyclone separator for gas–solid separation. The majority of the cleaned flue gas is filtered through a dust collector and discharged via a stack. A small portion, along with entrained solid material (circulating ash), is returned through a recirculation loop for continued reaction. This desulfurization process operates continuously to ensure emissions remain within regulatory limits [34].

As previously discussed, desulfurization occurs within the reactor. The internal flow and heat transfer characteristics are critical to the reactor's operational stability and desulfurization performance. In this study, a full-scale CFB-FGD reactor from the employed CFB-FGD system is selected as the subject for detailed investigation, with a focus on structural configuration, velocity field development, and thermal transport behavior. To reduce computational costs while leveraging geometric symmetry, only one-half of the reactor domain is modeled, as illustrated in Figure 2.

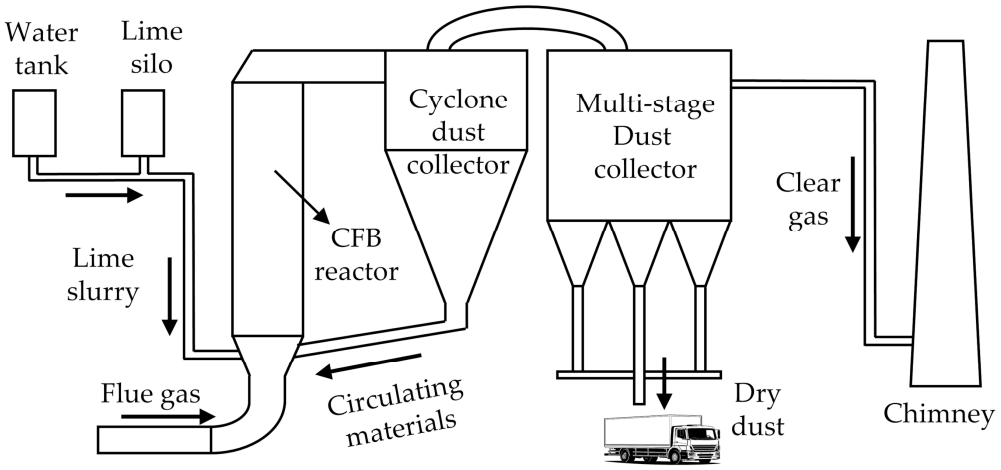


Figure 1. Circulating fluidized bed flue gas desulfurization technology.

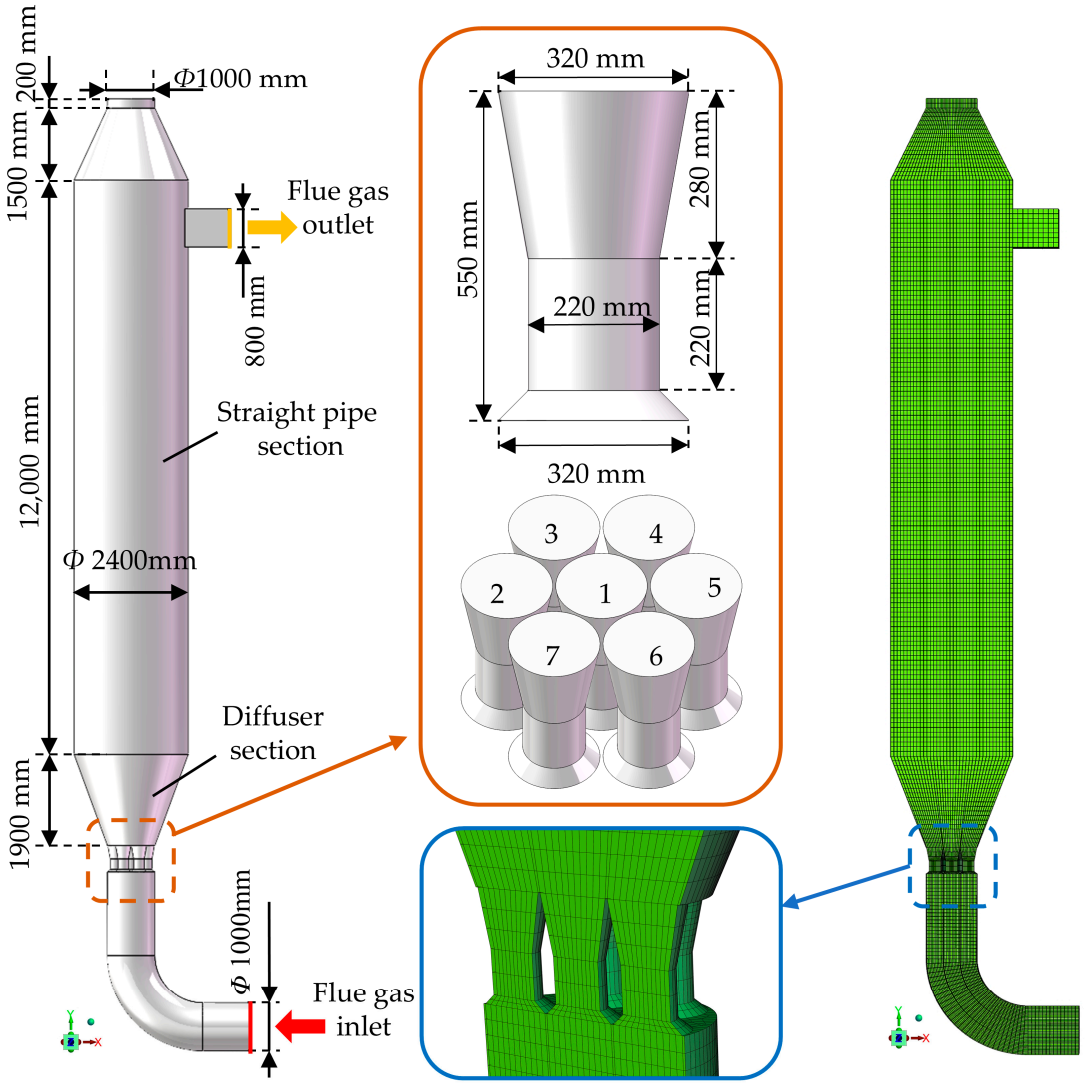


Figure 2. Physical model and mesh partitioning of CFB-FGD reactor.

The inlet duct geometry, featuring a characteristic "shrimp-shaped bend" structure commonly observed in industrial applications, is fully reproduced, with a total length of 13,200 mm and an inner diameter of 1000 mm. At the reactor base, a bundle of seven venturi tubes is installed in a layout consistent with actual operating conditions; for reference, each

venturi tube is individually labeled. Following passage through the venturi tube bundle, the flue gas is straightened and accelerated before entering the diffuser section, where desulfurization sorbents (e.g., lime, slaked lime), cooling water, humidification water, and chemical activators are injected. Additionally, circulating ash is introduced from the lower part of the straight pipe section to enhance solid-phase interactions. The main body of the reactor consists of a straight pipe section, which serves as the primary zone for gas–solid reactions between SO_2 and the sorbent. The fundamental reaction proceeds through the following stages: (1) SO_2 in the flue gas diffuses to the surface of the sorbent slurry droplets; (2) SO_2 dissolves into the liquid film on the droplet surface, forming H_2SO_3 and H_2SO_4; (3) these acids ionize into SO_3^{2-} and SO_4^{2-} within the liquid film; (4) sorbent particles dissolve in the liquid film and release Ca^{2+}; (5) SO_3^{2-} and SO_4^{2-} react with Ca^{2+} in the liquid film to form desulfurization products such as $CaSO_3$ and $CaSO_4$ [35,36]. However, ascharite ore roasting flue gas contains substantial B_2O_3 vapor and mineral dust. Both components may significantly affect desulfurization reaction progression and efficiency. Despite their potential influence, the underlying mechanisms—whether promotive or inhibitory—remain insufficiently understood due to limited prior research. Consequently, this study does not incorporate detailed modeling of the chemical reactions between flue gas constituents and sorbents. Instead, emphasis is placed on the investigation of flow behavior, interphase momentum exchange, and heat transfer characteristics within the reactor.

The geometric model of the CFB-FGD reactor was constructed using SolidWorks 2018. Mesh generation was performed using ICEM CFD 19.1. Local mesh refinement was applied in regions with rapid velocity changes, particularly in the venturi tube bundle and flue gas outlet zone.

In numerical simulations, increasing the mesh cell count generally improves accuracy. However, excessive mesh density also increases computational costs. Therefore, a grid independence study was conducted to achieve acceptable accuracy without significantly increasing the number of cells. Three mesh sizes were tested: a coarse mesh (1,232,397 cells), a medium mesh (1,848,590 cells), and a fine mesh (2,464,794 cells). The comparison showed that differences at identical monitoring points among the three meshes were minor and negligible. Consequently, to reduce computational effort, the coarse mesh with 1,232,397 cells was used for all simulations in this study.

2.2. Mathematical Model

Within the CFB-FGD reactor, the solid and liquid phases contained in the flue gas produced from ascharite ore roasting account for approximately 0.032% of the total volume. This value is far below the commonly accepted threshold of 15% required for applying the Discrete Phase Model (DPM). Accordingly, this study employed the Eulerian–Lagrangian formulation using the DPM [37]. In this framework, the gas phase is treated as a continuous medium and governed by Eulerian equations derived from conservation laws. The solid and liquid phases are modeled as discrete entities using a Lagrangian particle tracking method. Interphase coupling is implemented to account for momentum and energy exchanges between the phases. To simplify the numerical modeling and focus on key transport mechanisms, the following assumptions are introduced: (1) The flue gas is treated as an incompressible fluid; (2) chemical reactions inside the reactor—including desulfurization, catalytic enhancement, or inhibition—are neglected, and all solid-phase particles (including sorbents, dust, and circulating ash) are treated as inert; (3) the scattering effects of atomized water droplets and solid particles on the flue gas are assumed constant, with all particles modeled as uniform spheres [38]; and (4) heat exchange between the reactor walls and the external environment is not considered [39].

2.2.1. Continuous Phase Control Model

The continuity equation for fluids is as follows:

$$\frac{\partial \rho_f}{\partial t} + \nabla \cdot (\rho_f U_f) = S_M \tag{1}$$

where ρ_f is the fluid density, kg/m^3; U_f is the fluid velocity, m/s; and S_M is the mass source term, kg/(m^3·s).

The momentum equation for fluids is as follows:

$$\rho_f \left(\frac{\partial U}{\partial t} + (U \cdot \nabla) U \right) = -\nabla P + \nabla \cdot \tau + \rho_f g \tag{2}$$

where P is the fluid pressure, Pa; τ is the shear stress, Pa; and g is the acceleration due to gravity, typically taken as 9.81 m/s^2.

This study involves several key geometric structures, including the "shrimp-shaped bend", venturi tube, diffuser section, and gas injection disruptor. These structures significantly affect the flow and heat transfer within the reactor. The Realizable k-ε model offers advantages such as computational stability, easy convergence, and high efficiency. It can effectively handle rotating and high shear flows while requiring relatively lower mesh quality. Therefore, the Realizable k-ε model was adopted to describe turbulence in this study. The k equation and ε equation are described as follows [40]:

$$\frac{\partial (\rho k)}{\partial t} + \frac{\partial (\rho k U_i)}{\partial x_i} = \frac{\partial}{\partial x_i} \left[\left(\mu + \frac{\mu_t}{\sigma_k} \right) \frac{\partial k}{\partial x_i} \right] + P_k - \rho \varepsilon \tag{3}$$

$$\frac{\partial (\rho \varepsilon)}{\partial t} + \frac{\partial (\rho \varepsilon U_i)}{\partial x_i} = \frac{\partial}{\partial x_i} \left[\left(\mu + \frac{\mu_t}{\sigma_\varepsilon} \right) \frac{\partial \varepsilon}{\partial x_i} \right] + \rho C_1 S \varepsilon - \rho C_2 \frac{\varepsilon^2}{k + \sqrt{v\varepsilon}} - C_{1\varepsilon} \frac{\varepsilon}{k} C_{3\varepsilon} P_b \tag{4}$$

where k represents the turbulent kinetic energy, m^2/s^2; μ_t is the eddy viscosity, calculated as $\mu_t = \rho C_\mu k^2/\varepsilon$; $C_\mu = 1/(A_0 + A_s k U^*/\varepsilon)$; $A_s = \sqrt{6} \cos \phi$; U^* is the Characteristic velocity scale; P_k is the turbulent kinetic energy production term; P_b is the buoyancy production of turbulent kinetic energy; S is the mean strain rate, s^{-1}; ν is the kinematic viscosity, m^2/s. ε is the turbulent kinetic energy dissipation rate, m^2/s^3. The model constants are taken as: $C_{1\varepsilon}$ = 1.44, C_2 = 1.92, $C_{3\varepsilon}$ = 1.0, A_0 = 4.04 σ_k = 1.0, and σ_ε = 1.2.

2.2.2. Discrete Phase Control Equation

DPM is employed to simulate the motion of discrete particles—including desulfurization sorbents, cooling water droplets, humidification water, activators, and dust—within the reactor, accounting for the two-way coupling effects between the discrete particulate phase and the continuous gas phase. Four injection sources are defined for the discrete phase: fresh desulfurization sorbent injection, atomized water injection, circulating ash injection, and dust particles entrained in the flue gas from ascharite ore roasting.

During the simulation, the trajectories of discrete phase particles are calculated by solving the force balance acting on individual particles. In the Lagrangian reference frame, the particle motion is governed by the following force balance equation:

$$m_p \frac{dU_p}{dt} = m_p \frac{U_f - U_p}{\tau_p} + m_p \frac{g(\rho_p - \rho_f)}{\rho_p} + \vec{F} \tag{5}$$

where m_p is the particle mass, kg; U_p is the particle velocity, m/s; ρ_p is the particle density, kg/m^3; $\vec{F}$ represents additional body forces acting on the particle, N/m^3; $m_p \frac{g(\rho_p - \rho)}{\rho_p}$ is the drag force, N/m^3; and τ_p is the particle relaxation time.

τ_p is calculated using Equation (6):

$$\tau_p = \frac{\rho_p d_p^2}{18\mu} \frac{24}{C_d \mathrm{Re}_d} \tag{6}$$

where d_p is the particle diameter, m; Re_d is the particle Reynolds number and C_d is the drag coefficient.

Re_d is given by Equation (7):

$$\mathrm{Re}_d = \frac{\rho d_p |U - U_p|}{\mu} \tag{7}$$

C_d is given by Equation (8):

$$C_d = a_1 + \frac{a_2}{\mathrm{Re}} + \frac{a_3}{\mathrm{Re}} \tag{8}$$

where a_1, a_2, and a_3 are empirical constants, with $a_1 = 24$, $a_2 = 6$ and $a_3 = 0$.

The additional force term primarily accounts for the torque balance acting on the particles. Particle rotation constitutes an integral part of particle motion and can significantly influence their trajectories in the fluid flow. To incorporate rotational effects, it is necessary to solve an additional ordinary differential equation (ODE) that governs the angular momentum of the particles.

$$I_p \frac{d\vec{\omega}_p}{dt} = \frac{\rho}{2}\left(\frac{d_p}{2}\right)^5 C_\omega \left|\vec{\Omega}\right| \cdot \vec{\Omega} = \vec{T} \tag{9}$$

where I_p is the moment of inertia of the particle, kg·m^2; $\vec{\omega}_p$ is the angular velocity of the particle, rad/s; C_ω is the rotational drag coefficient, N·m·s/rad; $\vec{T}$ is the torque acting on the particle from the fluid domain (arising from the balance between particle inertia and drag) and $\vec{\Omega}$ is the relative angular velocity between the particle and the surrounding fluid, rad/s. $\vec{\Omega}$ is given by Equation (10):

$$\vec{\Omega} = \frac{1}{2}\nabla \times U - \vec{\omega} \tag{10}$$

For spherical particles, the moment of inertia is calculated as:

$$I = \frac{\pi}{60}\rho d^5 \tag{11}$$

For inert particles and atomized water droplets with temperatures below the evaporation point of water, the heat balance equation for the particles is expressed as follows [41,42]:

$$m_p c_{p,p} \frac{dT_p}{dt} = hA_p(T_\infty - T_p) + \varepsilon_p A_p \sigma\left(\theta_R^4 - T_p^4\right) \tag{12}$$

where $c_{p,p}$ is the specific heat capacity of the particle, J/(kg·K); A_p is the particle surface area, m^2; T_∞ is the temperature of the continuous phase, K; h is the convective heat transfer coefficient, W/(m^2·K); ε_p is the emissivity of the particle, σ is the Stefan–Boltzmann constant, 5.67×10^{-8} W/(m^2·K^4); θ_R is the radiation temperature, K; and T_p is the particle temperature, K.

When the droplet temperature reaches the evaporation temperature, the mass loss of the droplet is described by Equation (13):

$$m_{\mathrm{p}}(t+\Delta t) = m_{\mathrm{p}}t - N_i A_{\mathrm{p}} M_{\omega,i} \Delta t \tag{13}$$

where N_i is the molar flux of the vapor species, mol/(m^2·s); $M_{\omega,i}$ is the molar mass of species i, kg/mol.

$$m_{\mathrm{p}} c_{\mathrm{p}} \frac{\mathrm{d}T_{\mathrm{p}}}{\mathrm{d}t} = hA_{\mathrm{p}}(T_\infty - T_{\mathrm{p}}) + \frac{\mathrm{d}m_{\mathrm{p}}}{\mathrm{d}t} h_{\mathrm{fg}} + \varepsilon_{\mathrm{p}} A_{\mathrm{p}} \sigma \left(\theta_R^4 - T_{\mathrm{p}}^4\right) \tag{14}$$

where $\frac{\mathrm{d}m_{\mathrm{p}}}{\mathrm{d}t}$ is the evaporation rate of the droplet; h_{fg} is the latent heat of vaporization, J/kg.

The mass conservation equation for species transport is given by Equation (15) [39]:

$$\frac{\partial}{\partial t}(\rho Y_i) + \nabla \cdot (\rho U Y_i) = -\nabla \vec{J}_i + R_i + S_i \tag{15}$$

where Y_i is the mass fraction of species i, R_i is the rate of production of species i due to chemical reactions, kg/m^3·s; S_i is the additional source term due to the discrete phase, kg/m^3·s; and J_i is the diffusion flux of species i, kg/m^2·s. J_i arises from concentration gradients and, under turbulent flow conditions, is calculated by Equation (16):

$$\vec{J}_i = -\left(\rho D_{i,m} + \frac{\mu_t}{Sc_t}\right) \nabla Y_i \tag{16}$$

where Sc_t is the turbulent Schmidt number, set to 0.7, $D_{i,m}$ is the molecular diffusion coefficient of species i, m^2/s.

2.3. Boundary Conditions and Solution Methods

2.3.1. Boundary Conditions

Assuming a steady inflow of roasting flue gas, the inlet of the CFB-FGD reactor is defined as a velocity inlet boundary condition. The incoming flow is set to be perpendicular to the inlet surface, and the average velocity is calculated based on the measured volumetric flow rate and the inlet cross-sectional area. According to on-site measurements, the flue gas temperature at the inlet is specified as 443 K. The composition of the inlet gas is listed in Table 2, while dust is introduced as a discrete phase through an injection source, with detailed parameters provided in Table 3. At the inlet, discrete phase particles are assigned an escape boundary condition. Based on the calculated Reynolds number of the incoming flow, the flue gas is characterized as fully turbulent. The turbulence boundary conditions at the inlet are specified using the turbulence intensity and the hydraulic diameter, which are calculated by Equations (17) and (18), respectively:

$$I = 0.16(\mathrm{Re})^{1/8} \tag{17}$$

$$D = \frac{4A}{\mathrm{P}} \tag{18}$$

At the reactor outlet, a pressure outlet boundary condition was imposed, with the gauge pressure specified as 0 Pa. The backflow direction was set to be normal to the boundary. Based on field measurement data, the backflow temperature was initially specified as 65 °C and subsequently adjusted according to the simulation results. The mass fractions of N_2, CO_2, O_2, and H_2O in the backflow were determined from mass balance calculations. Given its extremely low concentration, SO_2 was set to 35 mg/m^3. At the outlet, discrete phase particles were defined with an escape boundary condition.

Table 3. Injection particles and physical properties [2].

Particles	ρ, kg/m^3	C_p, J/(kg·K)	λ, W/(m·K)	d_{min}, m	d_{max}, m	d_m, m	T, K	Q_p, kg/s
dust particles	2500	2170	1.62	2.5×10^{-6}	2.5×10^{-5}	7.8×10^{-6}	443	0.0001
atomized water droplets	998.2	4182	0.62	1.0×10^{-5}	1.0×10^{-4}	5.0×10^{-5}	283	0.3
circulating ash particles	2240	2000	1.73	1.0×10^{-6}	8.0×10^{-5}	3.6×10^{-5}	313	4
desulfurization sorbents	2240	2000	1.73	1.0×10^{-6}	1.0×10^{-4}	5.0×10^{-5}	283	0.2

[2] In this table: Q_p is the mass flow rate of the particles.

In practical applications, the reactor exterior is insulated with a layer of sufficient thickness, maintaining the outer surface temperature only 20–40 K above ambient. Consequently, heat dissipation through the walls has a negligible impact on the internal flow and temperature fields. Thus, following the aforementioned assumptions, the reactor wall is considered adiabatic, implying no heat or mass exchange with the external environment, and thus the heat flux through the wall is zero. The walls were stationary and were therefore modeled as no-slip wall boundaries [43]. For the continuous phase, the simulation results show that the dimensionless wall distance of the first near-wall cell (y^+) lies in the range of 30–300. This range satisfies the applicability requirements of the Standard Wall Function. Accordingly, the wall shear stress and the near-wall heat and mass transfer processes were modeled using the Standard Wall Function. For the discrete phase, the walls were specified as trap boundary conditions to simplify the treatment of particle–wall interactions and to focus on the dominant flow and heat transfer behavior. Under this assumption, discrete phase particles (e.g., droplets or sorbent particles) are trapped upon impingement on the wall and subsequently removed from the computational domain, representing particle deposition or adhesion in practical operation.

2.3.2. Solution Methods

During the calculation, DPM was employed to simulate the motion of various particulate species within the flue gas. Four particle injection sources were defined to represent dust, atomized water droplets, circulating ash, and the desulfurization sorbents. Particle trajectories were predicted based on the local mean velocity of the continuous phase, accounting for dispersion from instantaneous gas velocity fluctuations. To model these effects, a random walk model was utilized to determine the instantaneous gas velocity, and a stochastic tracking method was applied to capture the influence of turbulence on particle motion [44]. The discrete phase was coupled with the continuous phase by updating particle trajectories every 30 iterations of the continuous phase velocity field. The types of injected particles and their corresponding physical properties are listed in Table 3, where particle diameters are assumed to follow a Rosin–Rammler distribution. In this context, dust particles refer specifically to the particulate matter remaining in the flue gas after dedusting treatment.

The SIMPLE algorithm is employed to solve the flue gas velocity field using a pressure–velocity coupling approach. To balance computational accuracy, numerical stability, and resource efficiency, a second-order upwind scheme is applied for the discretization of both the momentum and energy equations. The convergence criteria require residuals below 10^{-3} for the continuity equation, velocity components, and k-ε turbulence equations. The energy equation residual must be less than 10^{-6}. Once the residuals of all governing equations meet these thresholds, the solution is considered to have converged.

3. Model Validation

As mentioned earlier, the internal flow in a CFB-FGD reactor is highly complex. To better understand the gas flow characteristics, Li [45] developed a cold-state flow simulation test platform for a CFB-FGD reactor featuring seven bottom-installed venturi tubes, structurally similar to the reactor investigated in this study. Using particle image velocimetry (PIV) technology, non-intrusive measurements of the internal velocity field were performed to evaluate the gas flow behavior within the venturi tubes. The main structure of the test platform is shown in Figure 3, which adopts a cylindrical geometry with dimensions of $\Phi 820 \times 4318$ mm. Seven venturi tubes are mounted at the reactor base, with their arrangement and numbering illustrated in Figure 3. Based on experimental parameters provided by the researcher, the mathematical model and numerical methods described in the previous section were applied to simulate the gas flow inside the reactor. Table 4 presents a comparison between the simulated and experimental volumetric flow rates for each of the seven venturi tubes. The simulation results exhibit good agreement with the experimental measurements, with the smallest relative error observed at venturi tube No. 2 (1.43%) and the largest at venturi tube No. 4 (7.56%). Moreover, the flow deviation induced by the "shrimp-shaped bend" in the inlet section was also accurately reproduced.

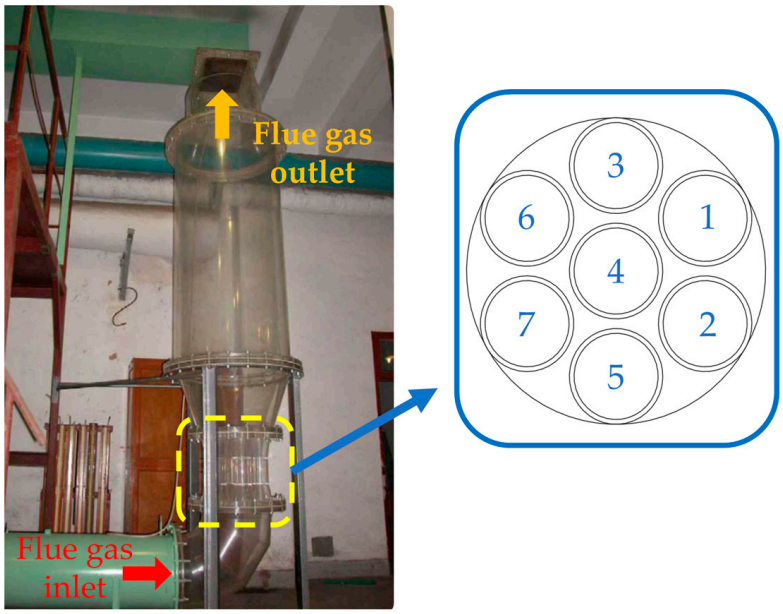


Figure 3. Schematic diagram of the desulfurization reactor test platform and venturi tube distribution [45].

Table 4. Comparison of the experimental and simulation values of the volumetric flow rates of 7 venturi tubes [45].

Venturi Tube Number	1	2	3	4	5	6	7
Experimental value (m^3/s)	0.339	0.344	0.291	0.291	0.290	0.259	0.259
Simulation value (m^3/s)	0.349	0.349	0.310	0.313	0.310	0.241	0.240
Relative error	2.95%	1.43%	6.53%	7.56%	6.90%	6.95%	7.34%

Figure 4 compares the simulated and experimentally measured flue gas velocity distributions along the y-axis at the intermediate cross-section of the reactor. The results show a high level of consistency between the numerical and experimental data, with the maximum deviation remaining below 10%.

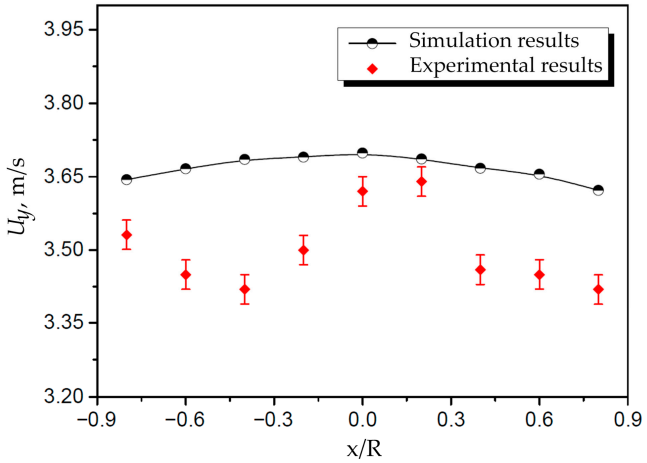


Figure 4. Comparison of the numerical simulation results and experimental results of the flue gas velocity inside the desulfurization reactor. (The horizontal axis represents the ratio of the x-coordinate to the reactor radius, while the vertical axis indicates the y-component velocity of the flue gas. The Cartesian coordinate system is established with its origin at the center of the outlet plane of venturi tube No. 4 (see Figure 3), and the vertical upward direction of the flue gas is defined as the positive y-component. Numerical simulation results are denoted by black semi-solid circles, and experimental measurements are represented by red solid diamonds.

To validate the applicability of the proposed mathematical model and numerical methods to heat transfer processes in a CFB-FGD system, the experimental data reported by Hong et al. [46] were adopted as a benchmark. A three-dimensional reactor model identical to that described in the literature was established, and numerical simulations were performed under the same operating conditions. The simulated area-averaged outlet temperature was then compared with the experimental measurements, as shown in Figure 5. Under the three investigated operating conditions, the simulated temperatures overpredict the experimental values by 7.4 °C, 3.3 °C, and 4.7 °C, respectively. This overprediction may be primarily attributed to the neglect of heat transfer between the reactor wall and the surrounding environment in the simulations.

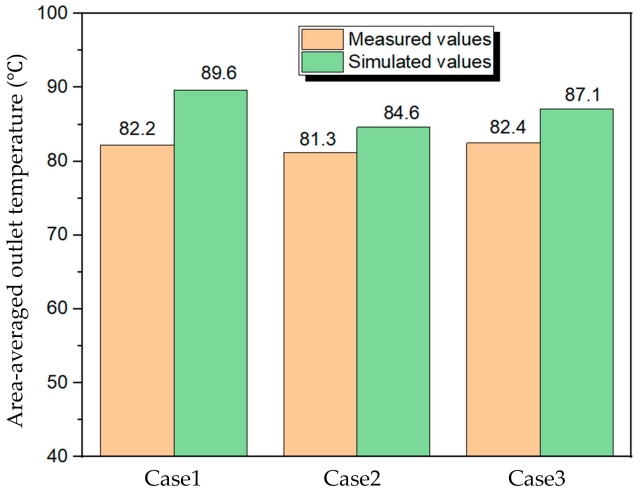


Figure 5. Comparison of simulated and experimental reactor outlet temperatures.

It should be noted that while the proposed mathematical model and numerical methods were partially validated against experimental data, the depth and breadth of this validation remain constrained by experimental limitations. Specifically, key performance parameters pertaining to heat transfer, chemical reactions, and mixing efficiency, such as

temperature distributions, species concentrations, and residence time distributions, were not experimentally verified. Consequently, the analyses and conclusions presented in this work should be viewed as an exploratory analysis of design trends and underlying mechanisms based on a hydrodynamically validated model, rather than a quantitative validation of the overall reactor performance.

4. Results Analysis

4.1. Implementing Differentiated Structural Dimension Adjustments for Venturi Tubes at Different Locations

The flow characteristics inside the CFB-FGD reactor are a critical factor affecting the desulfurization of flue gas from ascharite ore roasting. It is well established that the inlet structure plays a decisive role in inlet flow behavior and strongly influences the overall flow dynamics of the reactor. A properly designed inlet promotes uniform sorbent distribution, eliminates flow dead zones, maintains flow uniformity, reduces wall fouling, and enhances gas–solid contact.

Figure 6 presents the distribution of the y-component velocity of the flue gas within the CFB-FGD reactor before any modifications to the venturi tube configuration. In the original design, all seven venturi tubes share identical structural parameters: a throat diameter of 220 mm, a height-to-diameter ratio of 1, an outlet diameter of 320 mm, and an expansion angle of 20°. Five representative cross-sectional planes were selected for analysis. The origin of the Cartesian coordinate system is defined at the center of the outlet plane of venturi tube No. 1 (as shown in Figure 2). The upward vertical direction of flue gas flow is designated as the y-axis. As illustrated in Figure 6a, the flue gas experiences significant inertial deflection within the "shrimp-shaped bend" section of the inlet pipe. This deflection is not mitigated after acceleration through the venturi tubes. As a result, a pronounced deviation of the flue gas stream occurs inside the reactor. The y-component velocity increases markedly in regions far from the bend, while it decreases significantly in regions closer to the bend. As the flue gas continues to ascend, the degree of this velocity field non-uniformity gradually diminishes. Figure 6b–d indicate that the asymmetric velocity profile persists throughout the bed region from 0 to 6 m in height. The velocity distribution becomes relatively uniform only beyond 8 m. Furthermore, as shown in Figure 6a, the pressure imbalance caused by the velocity deviation induces recirculation zones in both the diffuser section and the upper regions of the reactor.

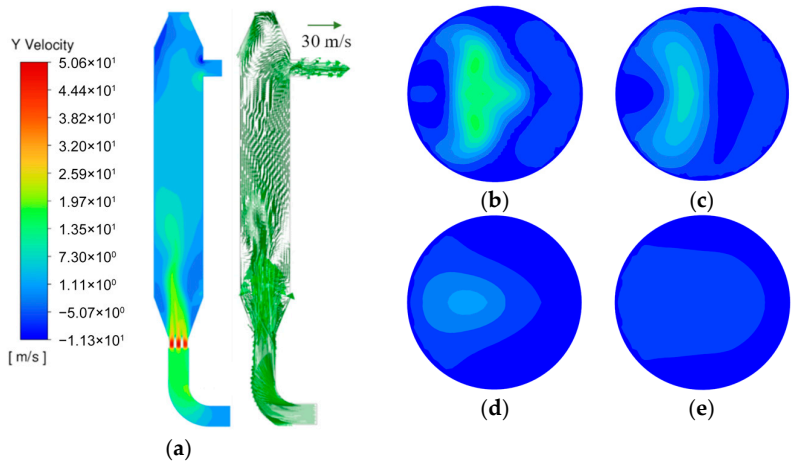


Figure 6. Distribution of y-component velocity component of flue gas in the reactor before adjustment: (**a**) z = 0 m; (**b**) y = 2 m; (**c**) y = 4 m; (**d**) y = 6 m; (**e**) y = 8 m. (As illustrated in Figure 2, the origin of the Cartesian coordinate system is defined at the center of the outlet plane of venturi tube No. 1, with the vertical upward direction of the flue gas designated as the y-axis).

Figure 7 shows the y-component velocity distribution in the middle cross-section of the throat of the venturi tube before adjustment. The y-component velocity near the inner side of the bent tube is significantly lower than that of other venturi tubes. Figure 8 shows the variation in the y-component velocity along the central axis of each venturi tube. As can be seen from the figure, there are significant differences in the y-component velocity along the central axis among different venturi tubes. The curve for venturi tube No. 5 is at the lowest position, while that for No. 3 is at the highest. Due to the influence of the "shrimp-shaped bend", the inlet velocity of the No. 5 venturi tube is relatively low. After acceleration through the inlet contraction section, the difference between it and the other venturi tubes becomes increasingly evident. By the time the flow reaches the outlet, the relative deviation reaches approximately 20%, which is the direct cause of the asymmetric distribution of the flue gas velocity field within the reactor.

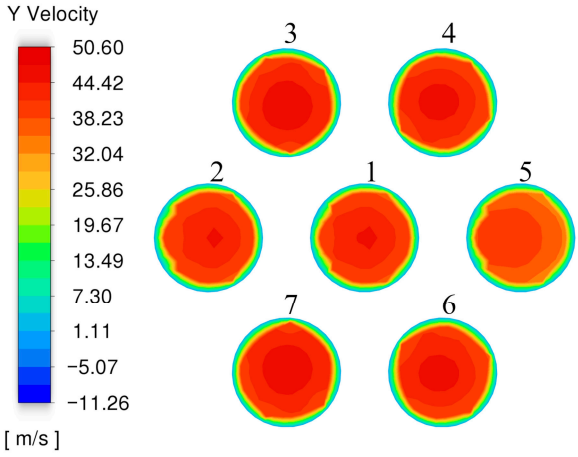


Figure 7. Contour plot of the y-component velocity distribution in the cross-section of the venturi tube throat (the numbers 1 to 7 in the figure represent venturi tubes labeled 1 to 7, respectively; see Figure 2).

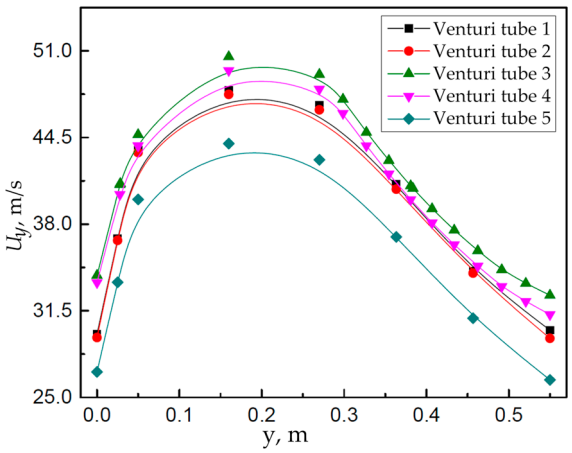


Figure 8. Changes in y-component velocity along the center axis of the venturi tube (The numbers 1 to 5 in the figure represent venturi tubes 1 to 5, respectively. Due to the symmetry of the structure, venturi tubes 6 and 7 are not shown. See Figure 2).

As previously discussed, the "shrimp-shaped bend" is the primary source of velocity field non-uniformity within the reactor. Although some researchers have proposed replacing this bent section with a straight pipe inlet to fundamentally eliminate the associated flow imbalance, such a redesign is practically infeasible due to constraints in the overall process layout. Further analysis reveals that the venturi tube configuration also exerts a substantial

influence on the internal flow distribution. Introducing differential structural parameters for venturi tubes at different positions generates local flow resistance variations, thereby regulating the velocity field. This approach essentially utilizes differentiated local flow resistance to compensate for the non-uniform momentum distribution, which is caused by the inlet "shrimp-shaped bend". This follows the principle of resistance balance in fluid networks. Therefore, systematic adjustment of the geometric dimensions of individual venturi tubes may effectively suppress the flow deviation induced by the inlet structure. In this study, we adopted a structural optimization strategy combining modifications of both the throat diameter and the outlet diameter of selected venturi tubes. The original venturi tube bundle consisted of seven tubes with identical structural parameters: a throat diameter of 220 mm, a throat height-to-diameter ratio of $L^2/D^2 = 1$, an outlet diameter of 320 mm, and an expansion angle of 20°. Through iterative trial-and-error simulations, an optimized configuration was obtained that effectively improved flow uniformity. Specifically, the throat diameter of venturi tube No. 3 was increased from 220 mm to 240 mm, while that of No. 5 was decreased from 220 mm to 200 mm. The outlet diameters of both tubes were reduced from 320 mm to 280 mm. The structural parameters of the remaining five tubes remained unchanged.

Figure 9 compares the distributions of the y-component velocity on the z = 0 cross-section before and after the geometric adjustment. The results clearly demonstrate that the uniformity of the y-component velocity within the reactor is significantly improved. Additionally, the symmetry of the velocity field in both the diffuser section and the straight pipe section is markedly enhanced following the structural modification. These findings indicate that position-specific optimization of venturi tube structural parameters is an effective method for improving the overall flow characteristics within the reactor.

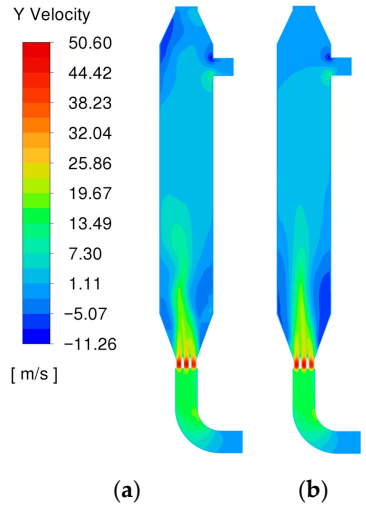


Figure 9. Distribution of the y-component of velocity in the z = 0 cross-section of the reactor before and after adjusting the venturi tube structural parameters: (**a**) before adjustment, (**b**) after adjustment.

A velocity distribution uniformity index (φ) was introduced to quantitatively evaluate the influence of variations in the venturi tube structural parameters on the flow field uniformity within the reactor. The index was calculated using the post-processing module of Fluent 19.1 and is defined as follows:

$$\varphi = 1 - \frac{1}{2\overline{u}A}\int_A |u - \overline{u}|dA \tag{19}$$

$$\overline{u} = \frac{\int udA}{\int dA} \tag{20}$$

where φ is the velocity distribution uniformity index across the investigated cross-section; u is the local velocity at an elemental area on the cross-section, m/s; $\overline{u}$ is the area-weighted average velocity, m/s; A is the total area of the investigated cross-section, m^2.

Figure 10 presents a comparison of the velocity distribution uniformity index along the bed height of the reactor before and after the differentiated adjustment of the venturi tube structural parameters. By definition, a higher value of the uniformity index indicates a more uniform velocity distribution over the corresponding cross-section. In general, a uniformity index greater than 0.70 is regarded as good, while values exceeding 0.85 are considered excellent. As shown in Figure 10, the flue gas velocity distribution in the reactor inlet region is highly non-uniform. With increasing bed height, the uniformity index gradually increases, indicating a progressively more uniform velocity distribution. It can also be observed that the curve corresponding to the adjusted venturi tube configuration consistently lies above that of the original configuration along the entire bed height. Prior to the structural adjustment, the uniformity index remained below 0.85 throughout most of the reactor, except for a small region near the top. In contrast, after the adjustment, the uniformity index increases from approximately 0.25 to 0.70 within the height range of 2.0–4.5 m, and further from 0.70 to 0.85 within the range of 4.5–6.2 m. Subsequently, the flow reaches the excellent uniformity regime and remains within this range thereafter. Both the regions corresponding to good and excellent velocity uniformity are substantially expanded following the structural modification.

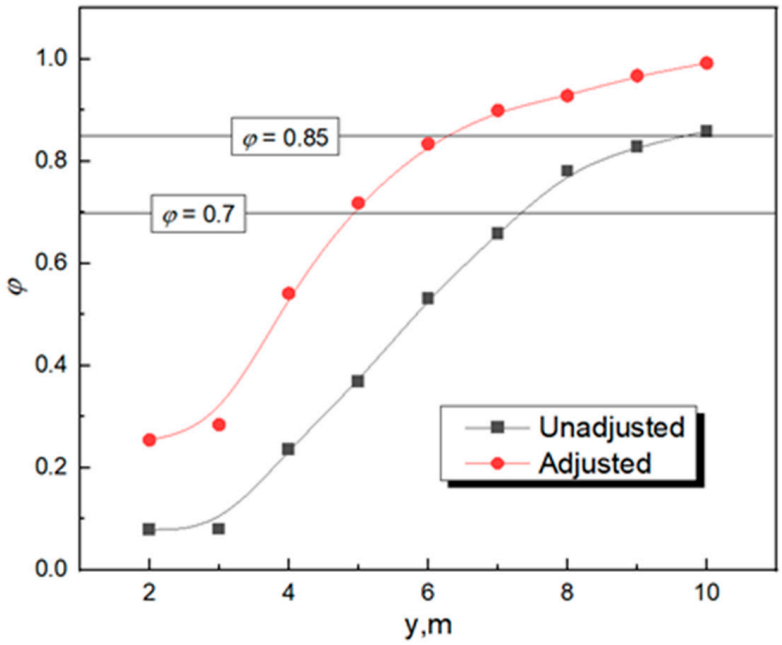


Figure 10. Comparison of the velocity distribution uniformity index along the bed height inside the reactor before and after adjustment of the venturi tube structural parameters.

Overall, compared with the original configuration, the adjusted venturi tube design significantly improves the global velocity distribution uniformity within the reactor, which is beneficial for enhanced mixing and more uniform reactions between the desulfurization sorbents and the flue gas.

4.2. Adjustment of Nozzle Installation Height

Key parameters influencing CFB-FGD desulfurization performance include the uniformity of both the velocity field and the temperature distribution within the CFB-FGD reactor. Practical experience indicates that the atomized water nozzle installation height plays a

critical role in shaping the internal temperature distribution. In this study, cone-shaped atomized water nozzles were positioned in the diffuser section of the reactor. Based on the optimized venturi tube structure, multiphase flow simulations were performed for nozzle installation heights (h) of 0.75, 1.00, 1.25, and 1.50 m. These simulations aimed to examine the effects of nozzle installation height on the temperature field and the corresponding uniformity index. Since droplet dynamics can influence flue gas flow, the velocity field was also analyzed in this section.

Figure 11 presents the temperature distribution at the z = 0 cross-section of the reactor for various atomized water nozzle installation heights. As shown, the flue gas generated from ascharite ore roasting is first accelerated and rectified by the venturi tubes before entering the diffuser section of the reactor. Atomized water droplets, sprayed from cone-shaped nozzles located in the diffuser section, are injected in the same direction as the flue gas. The atomized water droplets rapidly evaporate under the influence of the high-temperature flue gas. Most of the thermal energy is converted into the latent heat of vaporization, leading to a gradual temperature reduction from the bottom to the top of the reactor. It is evident from Figure 11 that the low-temperature region in the upper part of the straight pipe section consistently shifts toward the left side. The maximum temperature difference between the left and right regions reaches up to 20 K. Analysis suggests that this asymmetric temperature distribution is primarily caused by the sorbents' injection in the upper right part of the diffuser section. This deflects the atomized water droplet spray and the main flue gas stream toward the left side of the reactor. A comparison of different nozzle installation heights indicates that elevating the nozzles causes the low-temperature zone in the upper part of the straight pipe section to extend downward, thereby influencing the overall temperature distribution uniformity within the reactor. Despite the adjustments, the reactor exhibits a pronounced degree of thermal non-uniformity.

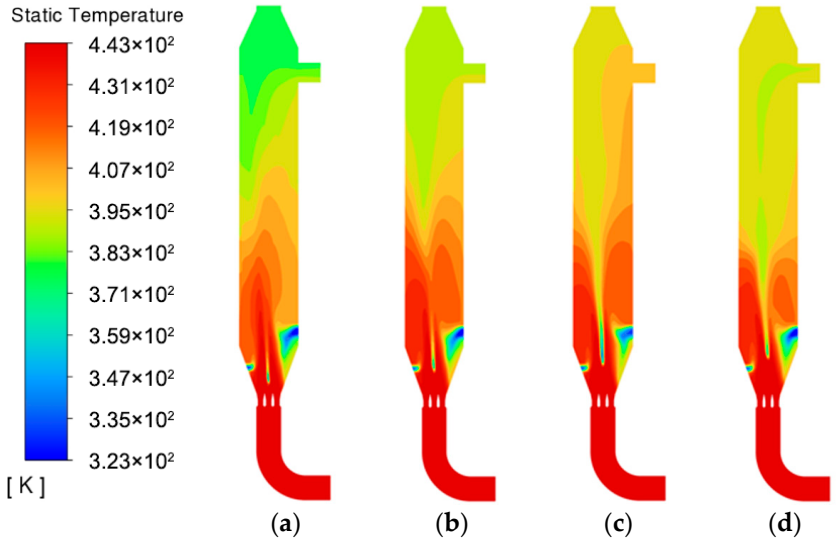


Figure 11. Temperature distribution on the reactor cross-section at z = 0 under different atomized water nozzle installation heights. (**a**) h = 0.75 m; (**b**) h = 1.00 m; (**c**) h = 1.25 m; (**d**) h = 1.50 m. (As illustrated in Figure 2, the origin of the Cartesian coordinate system is defined at the center of the outlet plane of venturi tube No. 1, with the vertical upward direction of the flue gas designated as the y-axis).

Non-uniform temperature distribution not only leads to uneven heating of the reactor wall but also adversely affects gas–solid heat transfer and desulfurization reactions inside the reactor. Following the quantitative approach used earlier for velocity uniformity analysis, a temperature distribution uniformity index (β) is introduced in this section to

evaluate the temperature distribution within the reactor. The mathematical expression of the index is given as follows:

$$\beta = 1 - \frac{1}{2\overline{T}A}\int_A |T - \overline{T}|dA \tag{21}$$

$$\overline{T} = \frac{\int TdA}{\int dA} \tag{22}$$

where β is the temperature distribution uniformity index across the investigated cross-section; T is the local temperature at an elemental area on the cross-section, K; $\overline{T}$ is the area-weighted average temperature over the cross-section, K.

As indicated by Equation (21), it can be seen that a larger value of the temperature distribution uniformity index indicates better temperature uniformity, and vice versa. As shown in Figure 12, the temperature distribution exhibits poor uniformity in the lower part of the straight pipe section, where the uniformity index is small. With increasing bed height, the temperature distribution uniformity index gradually rises, indicating that the temperature distribution becomes progressively more uniform along the height of the reactor. This trend is consistent with the velocity distribution described earlier.

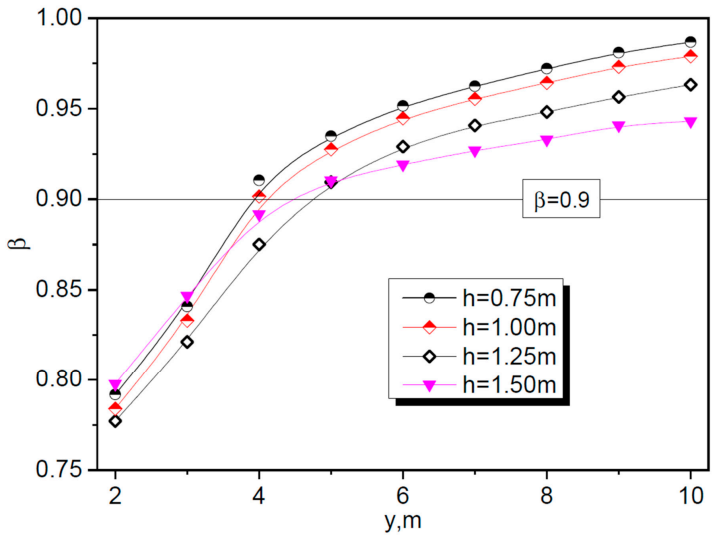


Figure 12. Effect of atomized water nozzle installation height on the temperature distribution uniformity index within the reactor. The horizontal axis in the figure represents the cross-sections at different heights of the reactor, while the vertical axis represents the temperature distribution uniformity index.

Figure 12 also shows that although the four curves follow similar trends, their magnitudes of variation differ significantly. In general, temperature uniformity is considered good when the uniformity index exceeds 0.85. For a nozzle installation height of h = 0.75 m, the index increases from 0.78 to 0.90 as the bed height rises from 2.00 m to 3.95 m. When h = 1.50 m, the index increases from 0.78 to 0.90 over the height range of 2.00 m to 4.92 m. Furthermore, at a fixed bed height of 10.0 m, reducing the nozzle installation height from 1.50 m to 0.75 m raises the temperature distribution uniformity index from 0.942 to 0.994. These results suggest that appropriately lowering the atomized water nozzle installation height can improve the temperature uniformity across the reactor cross-section to some extent. However, the nozzles should not be installed too low; otherwise, the desulfurization sorbents may agglomerate in the diffuser section, which would adversely affect fluidization.

Figure 13 illustrates the velocity distribution contours at the reactor's central cross-section (z = 0) under varying atomized water nozzle installation heights. In the diffuser section and the lower part of the straight pipe section of the reactor, the sorbent, circulating ash, and atomized water droplets are injected into the flue gas via nozzles. Under the influence of the high-velocity flue gas, these solid particles and atomized water droplets experience sufficient collision and mixing. This process leads to the formation of a uniform liquid film on the sorbent particle surfaces. Within this film, SO_2 dissolves and reacts ionically with the sorbent. This region exhibits the highest reaction rate and desulfurization efficiency in the entire CFB-FGD system. As shown in Figure 13, the ascharite ore roasting flue gas exhibits a velocity distribution characterized by a high-velocity core flow at the center, while the near-wall regions in the diffuser section and the lower part of the straight pipe section show significantly lower velocities, sometimes approaching zero. A comparison of different atomized water nozzle installation heights indicates minimal changes in the flue gas velocity distribution within the reactor. The impact of nozzle installation height adjustment is mainly localized near the sorbent jet zone at the upper right of the diffuser section, with negligible influence on other regions. This limited effect is attributed to the relatively low flow rate of atomized water compared to the flue gas, rendering small variations in nozzle installation height ineffective at altering the overall velocity field substantially.

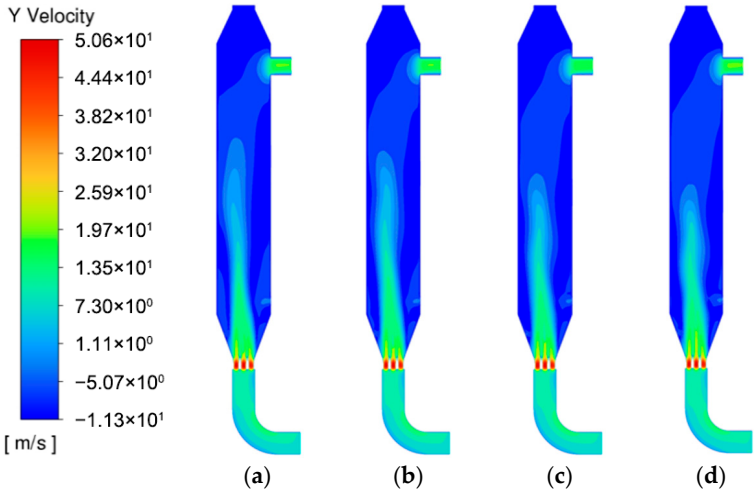


Figure 13. Velocity distribution within the reactor cross-section at z = 0 under different atomized water nozzle installation heights: (**a**) h = 0.75 m; (**b**) h = 1.00 m; (**c**) h = 1.25 m; (**d**) h = 1.50 m. (As illustrated in Figure 2, the origin of the Cartesian coordinate system is defined at the center of the outlet plane of venturi tube No. 1, with the vertical upward direction of the flue gas designated as the y-axis).

Figure 14 presents the distribution of the y-component velocity along the central axis of the reactor at different atomized water nozzle installation heights. As shown, within the reactor's straight pipe section, the main flow velocity of the ascharite ore roasting flue gas gradually decreases with increasing bed height, exhibiting a wavelike trend. A nearly horizontal plateau appears mid-curve, where the y-component velocity remains almost constant. With increasing nozzle installation height, this plateau region shifts downward, while the y-component velocity values show a gradual increase. Nevertheless, the overall influence of nozzle installation height on the velocity field within the reactor is limited. Based on these findings, it is clear that lowering the atomized water nozzle installation height from the original 1.50 m to 0.75 m enhances the temperature uniformity inside the reactor, thereby favoring the desulfurization reaction.

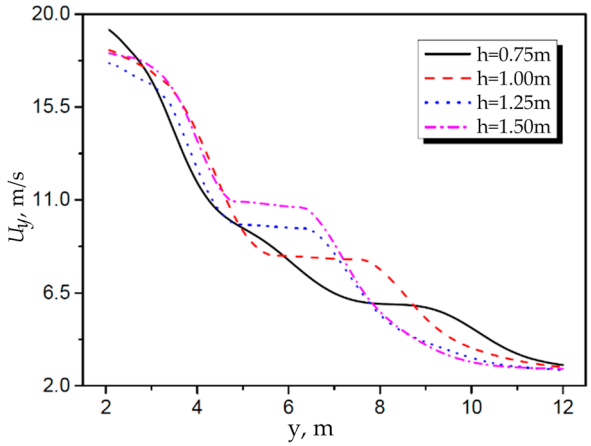


Figure 14. Distribution of y-component velocity at the center axis of the reactor under different nozzle installation heights. (The horizontal axis in the figure represents the height of the observation point on the reactor center axis, and the vertical axis represents the y-component velocity).

4.3. Installation of Gas Injection Disruptor in the Upper Part of the Straight Pipe Section

Based on the findings of the previous study, the regions of intense turbulent mixing and recirculation within the reactor are primarily located in the diffuser section and the lower part of the straight pipe section. In contrast, by the time the flue gas reaches the upper part of the straight pipe section, the flow becomes relatively stable and approaches a quasi-fully developed flow state. This flow behavior results in several unfavorable consequences. First, gas–solid mixing efficiency diminishes, hindering the progress of heterogeneous desulfurization reactions. Second, fewer collisions and reduced friction between desulfurization sorbents limit the exposure of fresh sorbent surfaces. Third, shortened travel paths lead to decreased residence time within the reactor. These factors collectively reduce the overall desulfurization efficiency of the CFB-FGD system. To mitigate these issues, this study proposes the installation of a gas injection disruptor—a turbulent gas curtain device—near the upper part of the straight pipe section. Accordingly, this section investigates the influence of the gas injection velocity from the disruptor on the internal velocity field, turbulent kinetic energy distribution, and the residence time of desulfurization sorbents within the reactor.

The configuration of the gas injection disruptor is shown in Figure 15 [47]. The disruptor body is a cylinder (diameter: 400 mm, height: 100 mm) installed coaxially in the upper part of the straight pipe section at an elevation of 10.5 m. Clean ambient air is used as the disruptor gas and is uniformly injected through an annular slit on the cylinder sidewall. The slit is located at the mid-height of the cylinder and is 10 mm in height. In the simulations, the disruptor gas temperature was set to 330 K. The gas injection velocity was varied at 15, 20, 25, and 30 m/s, corresponding to mass flow rates of 0.243, 0.324, 0.405, and 0.486 kg/s, respectively.

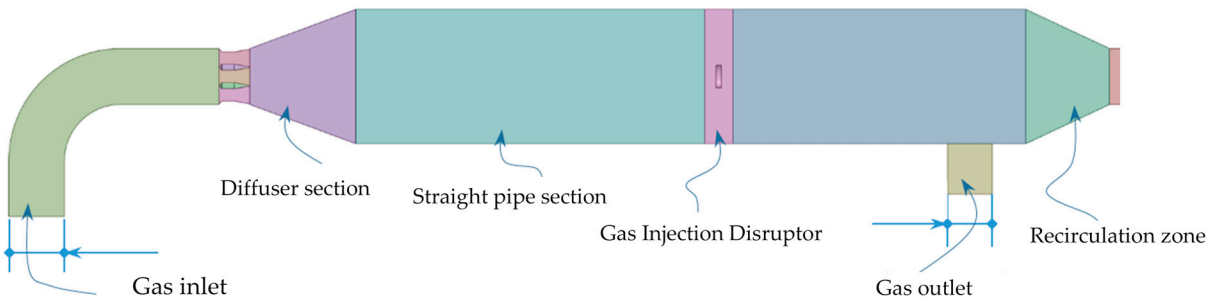


Figure 15. Installation position of the gas injection disruptor in the CFB-FGD reactor.

As shown in Figure 16, the velocity fields on the central cross-section (z = 0) of the reactor are compared for different gas injection velocities. In the absence of the disruptor (see Figure 13), the flue gas recirculation is primarily confined to the lower regions of the diffuser section and the straight pipe section. Upon installation of the gas injection disruptor, a vertical gas curtain is formed near the disruptor, oriented perpendicular to the reactor wall. This gas curtain deflects the upward flue gas from the reactor center toward the inner wall. Simultaneously, the wall-adjacent flue gas entrains the outer flow of the gas curtain and moves upward, forming a U-shaped velocity vector field above the disruptor. This interaction leads to the formation of two distinct recirculation zones, as illustrated in Figure 16, resulting in a new internal circulation loop for desulfurization sorbents in the reactor's upper section. Moreover, as the gas injection velocity increases, the U-shaped flow structure becomes more pronounced, the gas curtain expands, and recirculation intensifies. As a result, the recirculation zones above the disruptor grow in both size and strength. The gas curtain induces large-scale vortices in the main gas flow through momentum exchange. The intense shear and mixing effects are the key physical mechanisms for enhancing turbulence intensity and particle internal circulation in the upper part of the straight pipe section.

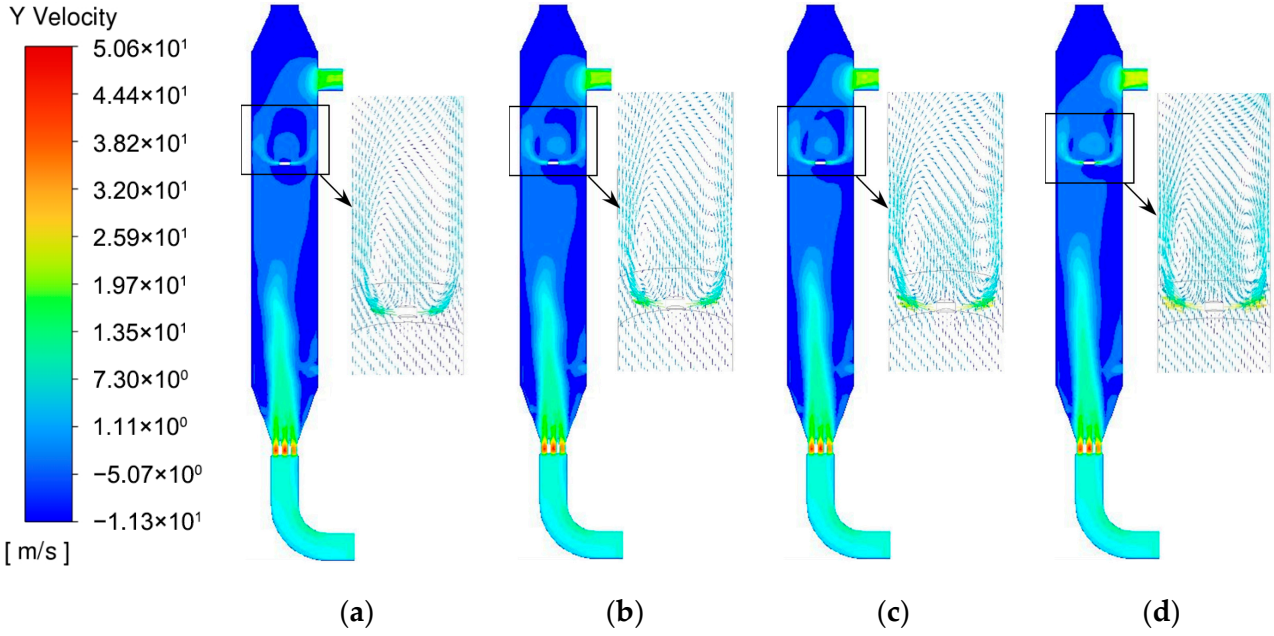


Figure 16. Velocity fields at the z = 0 cross-section of the reactor under different gas injection velocities: (**a**) u_0 = 15 m/s; (**b**) u_0 = 20 m/s; (**c**) u_0 = 25 m/s; (**d**) u_0 = 30 m/s.

Turbulent kinetic energy, a key indicator of turbulence intensity, is continuously dissipated into thermal energy during flow; its magnitude reflects the strength of turbulent mixing. Figure 17 presents the turbulent kinetic energy distribution on the central cross-section of the reactor (z = 0) under various gas injection velocities from the gas injection disruptor. As shown, high turbulent kinetic energy is primarily concentrated in the diffuser section, the lower part of the straight pipe section, the recirculation zones above the disruptor, and near the reactor outlet. Other regions exhibit relatively low turbulence intensity. The installation of the gas injection disruptor effectively increases the turbulent kinetic energy in the upper part of the straight pipe section, thereby enhancing gas-phase turbulence and promoting secondary mixing of particles. Under the same operating conditions, an increase in the gas injection velocity results in the expansion of high-turbulence regions and a corresponding rise in the average turbulent kinetic energy of the flue gas.

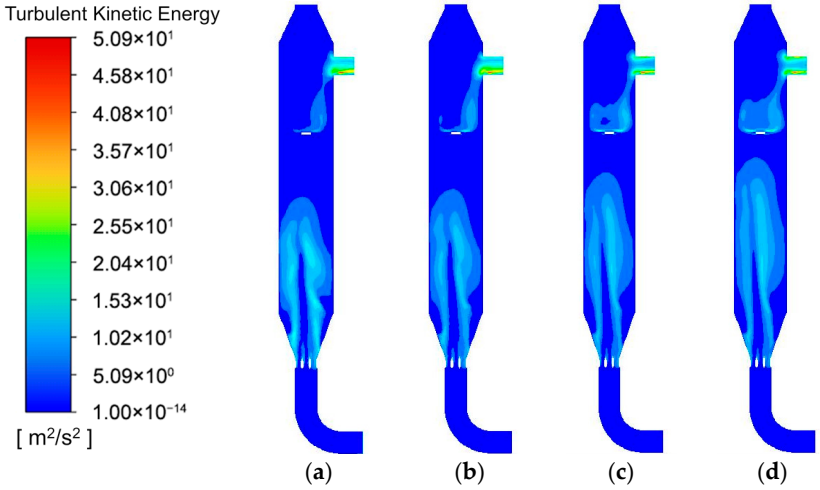


Figure 17. Turbulent kinetic energy distribution at the reactor's z = 0 cross-section under different gas injection velocities: (**a**) u_0 = 15 m/s; (**b**) u_0 = 20 m/s; (**c**) u_0 = 25 m/s; (**d**) u_0 = 30 m/s.

The residence time of the desulfurization sorbents refers to the average time that particles remain in the reactor before exiting and is a critical parameter affecting desulfurization efficiency, reactor design, and operational optimization. Table 5 summarizes the residence times of desulfurization sorbents under different gas injection velocities from the disruptor. The results indicate that the residence time increases with higher gas injection velocity, showing a clear positive correlation. In the absence of a disruptor, the average residence time is 4.256 s. With the disruptor installed, the residence time is significantly increased. Specifically, as the gas injection velocity increases from 15 m/s to 30 m/s, the average residence time increases from 6.751 s to 7.902 s.

Table 5. Residence time of sorbents in the reactor under different gas injection velocities of the gas injection disruptor.

u_0, m/s	Number of Tracked Particles (s)	Minimum Residence Time (s)	Maximum Residence Time (s)	Average Residence Time (s)
0	400	2.102	35.48	4.256
15		2.365	41.86	6.751
20		2.598	43.88	7.324
25		2.689	45.76	7.616
30		2.732	49.94	7.902

It should be noted that installing the gas injection disruptor in the upper part of the straight pipe section also introduces several adverse effects:

A dedicated air supply system for the disruptor will incur additional capital investment and operating costs. The major pressure loss of this system is concentrated at the disruptor annular slit and is proportional to the square of the flow rate. Calculations show that to maintain a gas injection velocity of 30 m/s (corresponding to an air mass flow rate of 0.486 kg/s), the local pressure loss at the nozzles alone reaches 600 Pa. Including the duct pressure loss (approximately 150 Pa) and the nozzle back pressure (about 100 Pa), the fan must provide a total pressure of about 1330 Pa, corresponding to a motor input power of approximately 835 W. The resulting energy consumption during long-term operation is considerable and represents an economic factor that must be considered in system optimization.

The injection of disruptor gas affects the flue gas composition in two ways. First, it dilutes the flue gas. Calculations indicate that at a disruptor gas injection velocity of 30 m/s, the injected gas volume accounts for about 5.38% of the total flue gas volume. Second, it

introduces additional O_2 from the air, which may alter the reaction atmosphere. However, because desulfurization primarily occurs in the middle and lower parts of the straight pipe section and the disruptor is installed in the upper part, these effects are relatively limited. If desulfurized recycled flue gas is used as the disruptor gas source, such impacts can be further reduced.

The injection of disruptor gas increases the total flue gas flow rate at the outlet of the desulfurization system. Therefore, the treatment capacity of the downstream flue gas exhaust system must accommodate this increment. However, simulation results indicate that the increase in total flue gas volume caused by the disruptor gas injection is limited ($\leq$5.38%), and the need for modifications to the existing exhaust system and the impact on its operating energy consumption are generally manageable.

The findings of this section indicate that installing a gas injection disruptor in the upper part of the straight pipe section can effectively enhance gas–solid interactions. This enhanced interaction, in turn, promotes the internal circulation of desulfurization sorbents and prolongs their residence time within the reactor. These improvements contribute to better adaptability of the CFB-FGD system to the flue gas produced by ascharite ore roasting.

5. Conclusions

This study employed numerical simulation to systematically analyze the multiphase flow and heat transfer characteristics of ascharite ore roasting flue gas within a CFB-FGD reactor. Based on the findings, key structural optimization strategies were proposed. From a hydrodynamic and thermal-field perspective, the primary objective was to improve internal velocity and temperature distribution uniformity. These improvements are hypothesized to be beneficial for enhancing desulfurization efficiency and mitigating borate deposition. The main conclusions are as follows:

(1) The conventional inlet structure leads to significant velocity field non-uniformity within the reactor. Differentiated adjustments to the structural parameters of venturi tubes at various positions effectively improved velocity distribution uniformity. After optimization, the overall velocity distribution in the reactor became significantly more uniform, promoting thorough mixing between the desulfurization sorbents and flue gas.

(2) The atomized water nozzle installation height is a key parameter affecting the reactor's temperature distribution. Reducing the height from 1.50 m to 0.75 m increased the temperature distribution uniformity index in the middle part of the straight pipe section by 5.5%.

(3) Installing a gas injection disruptor in the upper part of the straight pipe section effectively regulated the internal flow structure. As the gas injection velocity increased from 15 m/s to 30 m/s, the enhanced turbulence intensity induced by the disruptor increased the average residence time of desulfurization sorbents by 17.0%. This significantly strengthened gas–solid mixing.

(4) Implementation of the above optimization strategies synergistically reduced flow dead zones and low-temperature regions within the reactor. This provides an important theoretical basis and technical support for the optimization and industrial application of CFB-FGD technology for ascharite ore roasting flue gas.

Future work will focus on the following aspects. First, the coupling mechanism between multiphase flow and chemical reactions of ascharite ore roasting flue gas within the reactor should be investigated. Its quantitative impact on desulfurization efficiency will also be assessed. Second, the optimization strategies should be validated and iteratively refined at an industrial scale to establish reliable scale-up criteria. Furthermore, a systematic evaluation of influencing factors is necessary to improve the adaptability and

operational efficiency of CFB-FGD technology. These factors include fluctuations in flue gas composition and variations in key operational parameters.

Author Contributions: Conceptualization, M.F. and D.L.; Data curation, M.F.; Formal analysis, M.F., D.L. and S.Y.; Funding acquisition, M.F.; Methodology, M.F.; Resources, D.L. and S.Y.; Visualization, D.L. and S.Y.; Writing—original draft, M.F., D.L. and Z.W.; Writing—review and editing, M.F. and D.L. All authors have read and agreed to the published version of the manuscript.

Funding: This study is supported by the National Key Research and Development Program of China (No. 2017YFA0700300).

Data Availability Statement: Data are available from the corresponding author upon reasonable request.

Conflicts of Interest: The authors declare no conflicts of interest.

Nomenclature

Symbols

A	Area [m^2]
A_p	Particle surface area [m^2]
C_d	Drag coefficient
C_ω	Rotational drag coefficient [N·m·s/rad]
$c_{p,f}$	Fluid heat capacity [J/(kg·K)]
$c_{p,p}$	Particle heat capacity [J/(kg·K)]
D	Hydraulic diameter [m]
$D_{i,m}$	Molecular diffusion coefficient [m^2/s]
d	Diameter [m]
d_m	Particle average diameter
d_{min}	Particle minimum diameter
d_{max}	Particle maximum diameter
d_p	Particle diameter [m]
$\vec{F}$	Additional body forces acting on the particle [N/m^3]
g	Gravity acceleration [m/s^2]
h	Convective heat transfer coefficient [$W/(m^2 \cdot K)$]
h_{fg}	Latent heat of vaporization [J/kg]
I	Turbulence intensity
I_p	Moment of inertia of the particle [$kg \cdot m^2$]
J_i	Diffusion flux of species [$kg/(m^2 \cdot s)$]
k	Turbulent kinetic energy [m^2/s^2]
$M_{\omega,i}$	Molar mass of species [kg/mol]
m_p	Particle mass [kg]
N_i	Vapor species molar flux [$mol/(m^2 \cdot s)$]
P	Fluid pressure [Pa]
P	Wetted perimeter [m]
P_b	Buoyancy production term
P_k	Turbulent kinetic energy production term
Pr	Prandtl number
Q_p	Particles mass flow rate [kg/s]
Re_d	Reynolds number
R_i	Rate of production [$kg/(m^3 \cdot s)$]
S_i	Additional source term due to the discrete phase [$kg/(m^3 \cdot s)$]
S_M	Mass source term [$kg/(m^3 \cdot s)$]
T	Local temperature at the cross-section [K]
$\bar{T}$	Area-weighted average temperature [K]
$\vec{T}$	Torque
T_p	Particle temperature [K]
T_∞	Continuous phase temperature [K]
U_f	Fluid velocity [m/s]
U_p	Particle velocity [m/s]
U^*	Characteristic velocity scale
u	Local velocity at the cross-section [m/s]
$\bar{u}$	Area-weighted average velocity [m/s]
Y_i	Mass fraction

Greek Letters

α	Thermal Diffusivity [m^2/s]
β	Temperature distribution uniformity index
ε	Turbulent kinetic energy dissipation rate [m^2/s^3]
ε_p	Emissivity of the particle
θ_R	Radiation temperature [K]
λ	Thermal Conductivity [W/(m·K)]
μ	Dynamic Viscosity [Pa·s]
μ_t	Eddy viscosity [Pa·s]
ν	Kinematic viscosity [m^2/s]
ρ_f	Fluid density [kg/m^3]
ρ_p	Particle density [kg/m^3]
σ	Stefan–Boltzmann constant
τ	Shear stress [Pa]
τ_p	Particle relaxation time
φ	Velocity distribution uniformity index
$\vec{\Omega}$	Relative angular velocity [rad/s]
$\vec{\omega}_p$	Angular velocity of the particle [rad/s]

Subscripts

f	Fluid

S	Mean strain rate [s^{-1}]	p	Particle
Sc_t	Schmidt number	i	Species

References

1. Huang, W.; Liu, Y. Effect of Microwave Radiation on the Magnetic Properties of Ludwigite and Iron-Boron Separation. *J. Microw. Power Electromagn. Energy* **2021**, *55*, 93–106. [CrossRef]
2. Gao, W.; Zhang, F.; Peng, J.; Wang, Y.; Liu, S.; Yang, F. Effect of B_2O_3 on Stability of Magnetite Oxidation Process and Hematite Reduction Process. *Ironmak. Steelmak. Process. Prod. Appl.* **2025**, 03019233241309812. [CrossRef]
3. Dong, A.; Zhu, X.; Li, Z.; Kendall, B.; Li, S.; Wang, Y.; Tang, C. A Multi-Isotope Approach towards Constraining the Origin of Large-Scale Paleoproterozoic B-(Fe) Mineralization in NE China. *Precambrian Res.* **2017**, *292*, 115–129. [CrossRef]
4. An, J.; Xue, X. Life Cycle Environmental Impact Assessment of Borax and Boric Acid Production in China. *J. Clean. Prod.* **2014**, *66*, 121–127. [CrossRef]
5. Zhang, X.; Li, G.; Rao, M.; Peng, Z.; Zhong, Q.; Luo, J.; You, J.; Jiang, T. Co-Conversion Mechanisms of Boron and Iron Components of Ludwigite Ore during Reductive Soda-Ash Roasting. *Metals* **2020**, *10*, 1514. [CrossRef]
6. Zhu, Z.; You, J.; Zhang, X.; Li, G.; Wang, J.; Luo, J.; Rao, M.; Peng, Z.; Jiang, T. Recycling Excessive Alkali from Reductive Soda Ash Roasted Ludwigite Ore: Toward a Zero-Waste Approach. *ACS Sustain. Chem. Eng.* **2020**, *8*, 5317–5327. [CrossRef]
7. Bo, J.; Zhang, Y.; Zhang, Y. Leaching Magnesium Oxide in Boron Mud by Water with Pressurized CO_2. *Hydrometallurgy* **2017**, *171*, 142–148. [CrossRef]
8. Yu, T.; Sui, H.; Jiang, T.; Li, L.; Wen, J.; An, X. Preparation of Magnesium Oxysulfate Plates Using Boron Mud Solid Waste and Performance Evaluation. *J. Sustain. Metall.* **2025**, *11*, 1616–1624. [CrossRef]
9. Li, J.; Gu, X.; Wang, S.; Hu, Z.; Hu, Z.; Li, X. Study on the Preparation and Compressive Strength of Boron Mud-Based Basic Magnesium Sulfate Cement. *Materials* **2024**, *17*, 3301. [CrossRef] [PubMed]
10. Zhang, S.; Zhou, T.; Li, C.; Zhang, M.; Yang, H. Research Progress and Prospect of Fluidized Bed Metallic Ore Roasting Technology: A Review. *Fuel* **2024**, *378*, 132717. [CrossRef]
11. Zhong, Q.; Shen, H.; Yun, X.; Chen, Y.; Ren, Y.; Xu, H.; Shen, G.; Du, W.; Meng, J.; Li, W.; et al. Global Sulfur Dioxide Emissions and the Driving Forces. *Environ. Sci. Technol.* **2020**, *54*, 6508–6517. [CrossRef]
12. Chiang, T.-Y.; Yuan, T.-H.; Shie, R.-H.; Chen, C.-F.; Chan, C.-C. Increased Incidence of Allergic Rhinitis, Bronchitis and Asthma, in Children Living near a Petrochemical Complex with SO_2 Pollution. *Environ. Int.* **2016**, *96*, 1–7. [CrossRef]
13. Yu, H.; Shan, C.; Li, J.; Hou, X.; Yang, L. Alkaline Absorbents for SO_2 and SO3 Removal: A Comprehensive Review. *J. Environ. Manag.* **2024**, *366*, 121532. [CrossRef] [PubMed]
14. Deng, Y.; Ansart, R.; Baeyens, J.; Zhang, H. Flue Gas Desulphurization in Circulating Fluidized Beds. *Energies* **2019**, *12*, 3908. [CrossRef]
15. Gong, Y.; Yang, Z.-G. Corrosion Evaluation of One Wet Desulfurization Equipment—Flue Gas Desulfurization Unit. *Fuel Process. Technol.* **2018**, *181*, 279–293. [CrossRef]
16. Liu, P.; Yang, S.; Hu, J.; Wang, H. Numerical Analysis of SO_2 Removal Characteristics in Industrial Flue Gas Desulfurization Reactor by Spray Drying Adsorption. *Sep. Purif. Technol.* **2023**, *323*, 124475. [CrossRef]
17. Chen, Z.; You, C.; Liu, H.; Wang, H. The Synergetic Particles Collection in Three Different Wet Flue Gas Desulfurization Towers: A Pilot-Scale Experimental Investigation. *Fuel Process. Technol.* **2018**, *179*, 344–350. [CrossRef]
18. Yang, C.; de Falco, G.; Florent, M.; Bandosz, T.J. Empowering Carbon Materials Robust Gas Desulfurization Capability through an Inclusion of Active Inorganic Phases: A Review of Recent Approaches. *J. Hazard. Mater.* **2022**, *437*, 129414. [CrossRef]
19. Ji, W.; Yang, C.; Qu, G.; Zhou, J.; Chen, Y.; Tang, H.; Li, Z.; Xie, R.; Ning, P. Purification Mechanism of Corona Discharge Coupled with Dimethyl Sulfoxide Microemulsion for Simultaneous Desulfurization and Denitrification. *Sep. Purif. Technol.* **2022**, *300*, 121866. [CrossRef]
20. Ge, T.; Cai, C.; Min, F.; Zhang, M. Effects of Temperature and Frequency on the Dielectric Properties of Thiophene Compounds and Its Application in Coal Microwave-Assisted Desulfurization. *Fuel* **2021**, *301*, 121089. [CrossRef]
21. Flament, P.; Dolignier, J.C.; Martin, G. A Comprehensive Model of the Dry Desulphurisation Process. *Rev. Inst. Fr. Pét.* **1993**, *48*, 697–709. [CrossRef]
22. Saidi, M.; Basirat Tabrizi, H.; Grace, J.R. A Review on Pulsed Flow in Gas–solid Fluidized Beds and Spouted Beds: Recent Work and Future Outlook. *Adv. Powder Technol.* **2019**, *30*, 1121–1130. [CrossRef]
23. Li, H.; Zhang, H.; Li, L.; Ren, Q.; Yang, X.; Jiang, Z.; Zhang, Z. Utilization of Low-Quality Desulfurized Ash from Semi-Dry Flue Gas Desulfurization by Mixing with Hemihydrate Gypsum. *Fuel* **2019**, *255*, 115783. [CrossRef]
24. Che, X.; Wu, F.; Wang, J. Multiple Field Synergy Mechanism of the Desulfurization Process in the Intensified Spouted Beds. *Chem. Eng. J.* **2023**, *467*, 143521. [CrossRef]
25. Wang, Z.; Yang, C.; Zhu, L. Corrosion Analysis and Inhibition Studies in the Process of Natural Gas Wet Desulfurization. *Eng. Fail. Anal.* **2014**, *44*, 66–73. [CrossRef]

26. Chen, Z.; You, C.; Wang, H.; Xie, N. A Novel Technical Route Based on Wet Flue Gas Desulfurization Process for Flue Gas Dehumidification, Water and Heat Recovery. *Appl. Therm. Eng.* **2020**, *171*, 115102. [CrossRef]
27. Li, D.; Cai, R.; Zhang, M.; Yang, H.; Choi, K.; Ahn, S.; Jeon, C.-H. Operation Characteristics of a Bubbling Fluidized Bed Heat Exchanger with Internal Solid Circulation for a 550-MWe Ultra-Supercritical CFB Boiler. *Energy* **2020**, *192*, 116503. [CrossRef]
28. Mahasti, N.N.N.; Chang, K.-Y.; Lin, J.-Y.; Huang, Y.-H. Multi-Stage Calcium-Based Chemical Oxo-Precipitation Application to Treat Boron-Containing Flue Gas Desulfurization Wastewater from Coal-Fired Power Plant. *J. Environ. Chem. Eng.* **2024**, *12*, 113233. [CrossRef]
29. Goodarzi, F.; Swaine, D.J. Behavior of Boron in Coal During Natural and Industrial Combustion Processes. *Energy Sources* **1993**, *15*, 609–622. [CrossRef]
30. Chen, B.; Xia, Z.; Huang, L.; Hu, J. Ignition and Combustion Model of a Single Boron Particle. *Fuel Process. Technol.* **2017**, *165*, 34–43. [CrossRef]
31. Wu, J.; Yang, D.; Xu, M.; Ma, W.; Zhou, Q.; Xia, Z.; Lei, Y.; Wei, K.; Li, S.; Chen, Z.; et al. Boron Removal from Silicon Using Secondary Refining Techniques by Metallurgical Method. *Sep. Purif. Rev.* **2020**, *49*, 68–88. [CrossRef]
32. Jiao, G.; Xia, G.; Zhou, T.; Peng, M.; Wang, J. Transient Local Effects Analysis during Typical Accidents of a Heat Pipe Cooled Reactor. *Nucl. Eng. Des.* **2025**, *436*, 113988. [CrossRef]
33. Zhang, Y.; Li, R.; Zhang, B.; Miao, Y.; Guo, C.; Xia, G.; Peng, M. Design and Performance Analysis of 15MWth SCO2-Cooled Micro Reactor. *Nucl. Eng. Technol.* **2025**, *57*, 103863. [CrossRef]
34. Liu, P.; Wu, X.; Wang, Z.; Bo, Y.; Bao, H. Numerical Simulation Study on Gas–solid Flow Characteristics and SO_2 Removal Characteristics in Circulating Fluidized Bed Desulfurization Tower. *Chem. Eng. Process. Process Intensif.* **2022**, *176*, 108974. [CrossRef]
35. Cai, L.; Xu, Z.; Wang, X.; Bai, H.; Han, L.; Zhou, Y. Numerical Simulation and Optimization of Semi-Dry Flue Gas Desulfurization in a CFB Based on the Two-Film Theory Using Response Surface Methodology. *Powder Technol.* **2022**, *401*, 117268. [CrossRef]
36. Krammer, G.; Brunner, C.; Khinast, J.; Staudinger, G. Reaction of Ca(OH)2 with SO_2 at Low Temperature. *Ind. Eng. Chem. Res.* **1997**, *36*, 1410–1418. [CrossRef]
37. Yang, X.; Xi, T.; Qin, Y.; Zhang, H.; Wang, Y. Computational Fluid Dynamics–Discrete Phase Method Simulations in Process Engineering: A Review of Recent Progress. *Appl. Sci.* **2024**, *14*, 3856. [CrossRef]
38. Go, E.S.; Kim, B.-S.; Ling, J.L.J.; Oh, S.S.; Park, H.J.; Lee, S.H. In-Situ Desulfurization Using Porous Ca-Based Materials for the Oxy-CFB Process: A Computational Study. *Environ. Res.* **2023**, *225*, 115582. [CrossRef]
39. Chen, J.; Zhong, W.; Zhou, G.; Li, J.; Ding, S. Desulfurization Characteristics of Slaked Lime and Regulation Optimization of Circulating Fluidized Bed Flue Gas Desulfurization Process—A Combined Experimental and Numerical Simulation Study. *Chin. J. Chem. Eng.* **2024**, *73*, 163–175. [CrossRef]
40. Shih, T.-H.; Liou, W.W.; Shabbir, A.; Yang, Z.; Zhu, J. A New k-ε Eddy Viscosity Model for High Reynolds Number Turbulent Flows. *Comput. Fluids* **1995**, *24*, 227–238. [CrossRef]
41. Ye, X.; An, X.; Zhang, H.; Wang, S.; Guo, B.; Yu, A. Process Simulation on Atomization and Evaporation of Desulfurization Wastewater and Its Application. *Powder Technol.* **2021**, *389*, 178–188. [CrossRef]
42. Hong, M.; Xu, G.; Lu, P.; Huang, Z.; Miao, H.; Zhang, Y.; Ma, C.; Zhang, Q. CFD Analysis of the Spray Droplet Parameters Effect on Gas-Droplet Flow and Evaporation Characteristics in Circulating Fluidized Bed Desulfurization Tower. *Chem. Eng. Res. Des.* **2023**, *196*, 184–203. [CrossRef]
43. Tang, Q.; Wang, Q.; Cui, P.; Cao, W.; Hou, S. Numerical Simulation of Flue Gas Desulfurization Characteristics in CFB with Bypass Ducts. *Process Saf. Environ. Prot.* **2013**, *91*, 386–390. [CrossRef]
44. Lo, C.; Bons, J.; Yao, Y.; Capecelatro, J. Assessment of Stochastic Models for Predicting Particle Transport and Deposition in Turbulent Pipe Flows. *J. Aerosol Sci.* **2022**, *162*, 105954. [CrossRef]
45. Li, W. Experimental Investigation and Numerical Simulation on Cold Gas Flow Field in Multi-Venturi CFB-FGD. Master's Thesis, Southeast University, Nanjing, China, 2006. (In Chinese)
46. Hong, M.; Xu, G.; Lu, P.; Chen, F.; Sheng, G.; Zhang, Q. Numerical Simulation on Gas-Droplet Flow Characteristics and Spray Evaporation Process in CFB-FGD Tower. *Adv. Powder Technol.* **2023**, *34*, 104008. [CrossRef]
47. Xu, C.; Lai, Y.; Zhou, G.; Wu, D.; Xie, F.; Wang, Z. Study on flow behavior in a circulating fluidized bed FGD tower with spoiler. *J. Therm. Sci. Technol.* **2021**, *22*, 181–190. (In Chinese) [CrossRef]

Disclaimer/Publisher's Note: The statements, opinions and data contained in all publications are solely those of the individual author(s) and contributor(s) and not of MDPI and/or the editor(s). MDPI and/or the editor(s) disclaim responsibility for any injury to people or property resulting from any ideas, methods, instructions or products referred to in the content.